

Fabrication of reduced graphene oxide nanosheets doped PVA composite films for tailoring their opto-mechanical properties

Muhammad Aslam^{1,2} · Mazhar Ali Kalyar¹ · Zulfiqar Ali Raza²

Received: 16 March 2017 / Accepted: 10 May 2017 / Published online: 19 May 2017
© Springer-Verlag Berlin Heidelberg 2017

Abstract Laminar graphene nanosheets have raised passionate attention due to their incredible physico-chemical properties. Its wide-scale, high-yield production at low-cost has made it possible to produce top class promising versatile polymer nanocomposites. Reduced graphene oxide (RGO) nanosheets were incorporated to prepare optically tunable and high mechanical strength polymer nanocomposite films. RGO-doped poly(vinyl alcohol) (PVA) nanocomposite films were prepared via solution casting. Low level RGO doping significantly altered the structural, optical and mechanical properties of pure PVA films. Most of the band structure parameters like direct/indirect band gap, band tail, refractive index, dielectric constant, optical conductivity and dispersion parameters were investigated in detail for the first time. Tauc's, Wemple–DiDomenico, Helpin–Tsai and mixture rule models were employed to investigate optical and mechanical parameters. The applied models reinforced the experimental results in the present study. Advanced analytical techniques were engaged to characterize the nanocomposites films.

1 Introduction

Poly(vinyl alcohol) (PVA) is a distinguished polymer due to its biodegradable, biocompatible, hydrophilic and unique film formation and adhesive nature. It possesses good charge storage ability, large dielectric strength and exciting optical properties [1]. Its optical and mechanical properties can easily be improved by introducing small dopant quantity. Much more attention is diverted towards incorporation of inorganic nanomaterials into polymers because their combination provides an easy way to approach processable and stable nanocomposites, incorporating the promising features of both participants [2]. Carbon chain is the backbone of PVA matrix. The hydroxyl groups attached to this backbone are hydrogen bonding source that play the key role in upgrading composite formation [3]. The achievement of uniform dispersion of polymer nanocomposite is difficult due to the tendency of nanoparticles agglomeration [4]. Laminar carbon nanosheets of graphene have been reported as a milestone in different fields of engineering and science because of their unprecedented physico-chemical properties. The development on a large scale at a low cost and high yield enabled this amazing material to fabricate high strength polymeric nanomaterials. Isolated graphene nanosheets are not found in nature but functional graphene nanosheets can be prepared through different routes [5]. Graphene with 2D honeycomb structure is known to be one of the strongest materials [6]. It means that the graphene sheets may be considered as ideal reinforcement nanofiller for the polymer composite. The doping even at low concentration may enhance the performance of nanocomposite as compared to conventional one, provided the dispersion at molecular level is homogenous and load is transferred efficiently at nanosheets–polymer interface. Reduced graphene oxide (RGO) synthesized through hydrazine reaction of graphene oxide (GO) contains residual

✉ Muhammad Aslam
aslamfaridipk@gmail.com

✉ Zulfiqar Ali Raza
zarazapk@yahoo.com

¹ Department of Physics, University of Sargodha,
Sargodha 40100, Pakistan

² Department of Applied Sciences, National Textile University,
Faisalabad 37610, Pakistan

oxygen-functional groups. These oxygen-functional groups play an effective role in dispersion mechanism of composites. But the van der Waals forces among adjacent graphene nanosheets cause agglomeration, so the instability of dispersion takes place [7]. Such agglomerations may reduce reinforcement effect of dopant in nanocomposite. It is also reported in the literature that PVA resists the aggregation of nanoparticles [8]. To get true homogenous dispersion of nanocomposite at molecular level, it is suggested to use water as a common solvent. Excellent interfacial adhesion and efficient load transfer at nanosheets–polymer interface are also recommended for homogenous dispersion. The most realistic approach in this regard might be to enhance hydrogen bonding in nanocomposites.

In the present study, GO was prepared via modified Hummer's method. The RGO–PVA nanocomposite films were prepared using solution casting method, which was accomplished by adding hydrazine monohydrate into GO–PVA solution. This method is the cost effective and efficient in preventing restacking the nanosheets into polymer. Structural, optical and mechanical properties of PVA were modified using RGO nanosheets as nanofiller. The novelty of the present work is the investigation of band structure parameters in detail for the first time. Tauc's and Wemple–DiDomenico ($W-D$) models were used to investigate band gap and dispersion of refractive index of nanocomposites, respectively. Hsueh–Tsai ($H-T$) and mixture rule models were employed to ascertain Young's moduli of the nanocomposites. The applied models reinforced the experimental results in the present study. Optically tunable and strong nanocomposites of the present study might be strong candidates in designing the optoelectronic devices. The nanocomposite films were analyzed using X-ray diffraction (XRD), UV–visible spectroscopy, Fourier transform infrared (FTIR) spectroscopy, scanning electron microscopy (SEM), field emission scanning electron microscopy (FE SEM) and tensile testing.

2 Materials and methods

2.1 Materials

GO nanosheets were prepared according to the previous study [9]. Poly(vinyl alcohol) 70–90% hydrolyzed (average molecular weight 30,000–70,000) and hydrazine monohydrate (98%) was procured from Sigma-Aldrich, and deionized water (18 M Ω) from Millipore System, USA.

2.2 Preparation of RGO–PVA nanocomposite films

The RGO–PVA nanocomposite films were prepared through solution casting process [6]. The GO dispersion

was prepared in distilled water using sonication bath for 3 h. PVA solution was prepared in distilled water under magnetic stirring at 60 °C for 3 h. The GO dispersion was poured slowly into PVA solution and further stirred for 1 h. Pure hydrazine monohydrate as 1 ml was poured into it. The dispersion was placed on magnetic stirrer at 100 °C using an oil bath for 24 h. After completion of reduction reaction, dispersion was again sonicated at 25 °C for 1 h. The dispersion was cast on clean glass Petri plate and kept at 25 °C for drying. The concentrations of RGO in separate nanocomposite films were set as 0, 0.002, 0.004, 0.008, 0.012 and 0.020% (w/w) with respect to pure PVA contents. After drying, the prepared nanocomposite films were detached from the glass Petri plates. The films were cut into appropriate sizes for subsequent analyses. The average thickness of the nanocomposite films was $150 \pm 10 \mu\text{m}$.

2.3 Characterization techniques

An X'Pert PANalytical XRD machine was employed for the determination of the presence of RGO nanosheets in PVA matrix and relative crystallinity of the prepared nanocomposite films. The XRD machine fitted with $\text{CuK}\alpha$ (1.5406 Å) source was operating at 40 mA and 45 kV. The nanocomposite films were scanned in 2θ range of 10° – 45° at $0.5^\circ \text{min}^{-1}$ scan rate. To examine the interaction of RGO nanosheets with PVA matrix, FTIR spectra were recorded using a Perkin-Elmer Spectrum Two spectrometer (Buckinghamshire, UK). The instrumental spectral resolution was 0.5cm^{-1} . The phase morphological analysis of the samples was performed using Tescan Vega TS 5130 SEM machine. The samples were gold coated prior to SEM scanning, using sputter coater (Blazers Union FL 9496). The micrographs of the samples were also captured using JEOL JSM 7500 F field emission electron microscope (FE SEM). For the measurements of optical parameters, UV–visible spectrum was recorded with a UV-2800 BMS spectrophotometer (Biotechnology Medical Services, USA) in the scanning range 200–800 nm. Mechanical properties of the prepared samples were studied using an Instron 4302 Universal Testing Machine (USA) furnished with 5 kN load cell. The measurements were taken at a crosshead speed of 100mm min^{-1} at 25 °C. The prepared films were shaped into rectangular strips of width 50 mm. Five strips of each sample were tested on the machine and the averaged reading was used in calculations.

2.4 Optical parameters

The simplest and direct source of exploring the band structure including optical band, refractive index and optical conductivity of a nanocomposite is its optical absorption spectrum [10]. The abrupt change in absorption

is called absorption edge. This fundamental parameter is important for evaluation of band gap and transition nature [11]. The absorption coefficient (α) of the nanocomposite films can be calculated using absorption spectroscopy [12]:

$$\alpha = 2.303 \frac{A}{t}, \quad (1)$$

where A is the absorbance and t is the thickness of nanocomposite film. The electronic transitions take place close to absorption edge [13]. The direct and indirect energy band gap of an optical transition can be calculated from Tauc's plot [14]:

$$\alpha h\nu = B(h\nu - E_g)^\kappa, \quad (2)$$

where h is the Planck's constant, ν is the incident photon frequency, the factor B depends on the probability of inter-band transition that is supposed to be constant within the optical band, $h\nu$ is the energy of incident photon, E_g is the energy band gap and index κ defines nature of transition. Index κ is correlated to density of states distribution; it may take values of 1/2 for direct allowed or 3/2 for direct forbidden transitions. Index κ may also take values of 2 for indirect allowed or 3 for indirect forbidden transitions [15].

When absorption coefficient is low, i.e., $\alpha < 10^4 \text{ cm}^{-1}$, it can be defined as Urbach empirical relation [16],

$$\alpha = \alpha_0 \exp\left(\frac{h\nu}{E_u}\right), \quad (3)$$

where α_0 is a constant and E_u is Urbach energy or band tail width. For poor crystalline materials, the created localized states of energy are extended into band gap region causing the decrease in the band gap. Equation (3) can easily be modified into straight line equation:

$$\ln \alpha = \ln \alpha_0 + \frac{h\nu}{E_u}. \quad (4)$$

The Urbach energy can be calculated using the slope of straight line, by plotting $\ln(\alpha)$ against $(h\nu)$. The refractive index (n) of a material can be calculated using a relation containing reflectance (R) and extinction coefficient (K) [17]:

$$n = \left(\frac{1+R}{1-R}\right) + \left[\frac{4R}{(1-R)^2} - K^2\right]^{1/2}. \quad (5)$$

The extinction coefficient is related with absorption coefficient as: $K = \alpha\lambda/4\pi$.

The real part (ϵ_r) and imaginary part (ϵ_i) of optical dielectric constant can be tabulated using equations $\epsilon_r = n^2 - K^2$ and $\epsilon_i = 2nK$, respectively. The relationship for calculating the optical conductivity (σ) is related with refractive index, absorption coefficient and velocity of light in vacuum (c) as $\sigma = n c \alpha/4\pi$.

2.5 Mechanical parameters

RGO, one of the strongest materials, can reinforce the mechanical properties of polymer even at very low level loadings. The mechanical performance of samples can be improved using greater aspect ratio RGO nanosheets, homogenous suspension of nanofiller into polymer and good nanofiller-polymer interfacial bonding. The mechanical properties of the samples were accessed via stress-strain curves and linear fitting of load-gauge length curves. The H-T and mixture rule modeling curves were drawn to estimate a Young's moduli of the present study.

3 Results and discussion

3.1 XRD analysis

An XRD pattern could be employed to detect the presence of individual nanosheets and to calculate relative crystallinity of the nanocomposites [6]. Figure 1a indicates the XRD fingerprints of both pure PVA and RGO-PVA nanocomposite films. The PVA has a characteristic peak at $2\theta = 20.07^\circ$ at (101) reflection plane, whereas a broad trace of RGO nanosheets was observed at $2\theta = 23.19^\circ$ in our previous study [9]. After loading the RGO nanosheets into PVA matrix, the characteristics peak of RGO was dispersed and the nanocomposite films showed a single enlarged peak at about $2\theta = 20^\circ$. The same behavior was observed in all RGO-PVA nanocomposites. This confirmed a uniform dispersion and exfoliation of RGO nanosheets into PVA matrix at molecular level without restacking and with somewhat disorder and loss in its structural regularity [18]. The nature of pure PVA matrix is semi-crystalline. The origin of the crystallinity is a strong intermolecular hydrogen bonding in PVA chains. The peak strength of nanocomposites depends on the number of packed polymer chains [19]. The crystallinity has the direct influence on polymer properties. Its higher value increases secondary bonding and improves the strength of the polymer and creates brittleness [20]. Crystallinity of PVA nanocomposite plays an important role on its mechanical performance because of semi-crystalline nature of PVA. The relative crystallinity (χ_c) of RGO-PVA nanocomposites was calculated using Eq. (6) [21]:

$$\chi_c = \frac{A_{\text{crys}}}{A_{\text{amor}} + A_{\text{crys}}} \times 100, \quad (6)$$

where A_{crys} and A_{amor} are the areas of crystalline and amorphous regions, respectively. The amorphous and crystalline regions can be separated in main XRD peak using Origin software. Figure 1b represents the relative crystallinity of different RGO-PVA nanocomposite films at different loadings. The inset of Fig. 1b shows two Gaussian peaks

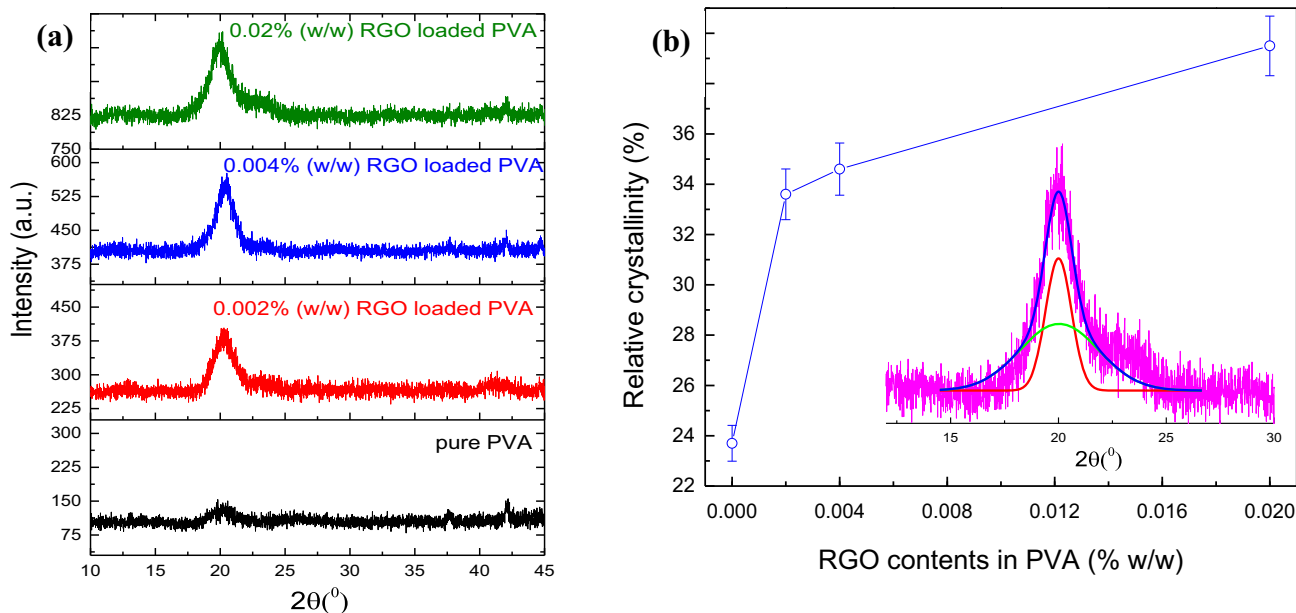


Fig. 1 **a** XRD patterns of pure PVA and RGO–PVA nanocomposite films, and **b** relative crystallinity of RGO–PVA nanocomposite films at different loadings. The *inset* shows Gaussian fitting XRD peak of

0.020% (w/w) nanocomposite. *Green, red and blue curves* represent amorphous, crystalline and sum of both the regions, respectively

fitted in the main X-ray diffraction peak of 0.02% (w/w) RGO loaded PVA nanocomposite film. The broad (green color) and narrow (red color) Gaussian peak was termed as amorphous and crystalline regions, respectively (Fig. 1b). The areas under crystalline and amorphous regions were calculated using Gaussian profile of the peaks. The relative crystallinity (%) of the nanocomposites was calculated using Eq. (6). The crystallinity is improved when the peak intensity of the nanocomposite is increased by increasing the nanofiller loadings [22]. The relative crystallinity of pure PVA was calculated as 23.7%. Sharma et al. [21] calculated relative crystallinity of pure PVA as 25.2% using Eq. (6). Figure 1b shows the increasing trend of relative crystallinity with loadings. After adding 0.020% (w/w) RGO nanosheets, the relative crystallinity was increased up to 39.5%. The variation in the slopes of relative crystallinity of the nanocomposites is due to the role of inorganic nanofiller as nucleation center [23, 24]. Thus, on increasing the incorporation of RGO nanosheets into PVA matrix, the relative crystallinity increases. This increase in crystallinity might also be due to extra-ordinary mechanical strength of individual RGO nanosheets that could effectively restrict and order the chain arrangement of polymer [25]. The XRD patterns depict that the nanocomposites might have improved mechanical strength with brittleness in nature.

3.2 FTIR analysis

The performance of the nanocomposite could be efficiently improved by robust interaction at nanofiller–polymer

matrix interface. It is an established fact that –OH and –C–OH stretching vibrations play the key role in hydrogen bond formation and in interfacial interactions [20]. To estimate the nanofiller interaction with polymer, the samples' spectra were recorded and analyzed. Figure 2 indicates the FTIR spectra of pure PVA and RGO doped PVA samples. A broad absorption peak, extended between 3000 and 3500 cm^{-1} , showed –OH symmetrical stretching and revealed the existence of robust intermolecular hydrogen bonding [26]. The absorption peaks at 2800–3000 and 1300–1500 cm^{-1} were attributed to –CH₂ stretching and CH/CH₂ deformation vibrations, respectively. The absorption peak at 1723 cm^{-1} of pure PVA was designated as stretching vibrations of C=O group [25]; however, it disappeared with the addition of RGO nanosheets. The –OH stretching vibrations peak at 3274 cm^{-1} of nanocomposites shifted toward lower wavenumbers by loading RGO nanosheets in the matrix. The peak shifting phenomenon was associated with the hydrogen bond formation between PVA chain and RGO sheets and it could be credited to the dissociation of hydrogen bonding in hydroxyl group of PVA [27, 28]. The hydrogen bond reduction in –OH group of PVA matrix might be due to the addition of RGO nanosheets. By adding more RGO nanosheets, the hydrogen bonds of PVA chain reduced furthermore, thereby shifting the peak wavenumber toward the lower values. The reduction of hydrogen bonding in –OH group of PVA causes the formation of hydrogen bond between PVA chain and RGO sheets. This is the property enhancement key factor [22]. The significant improvement

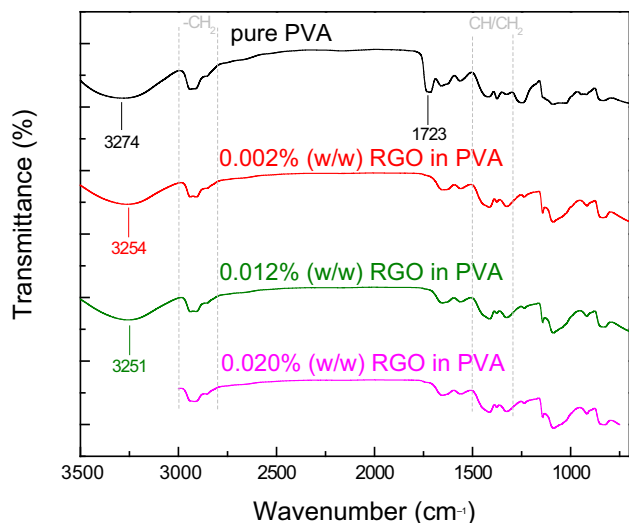


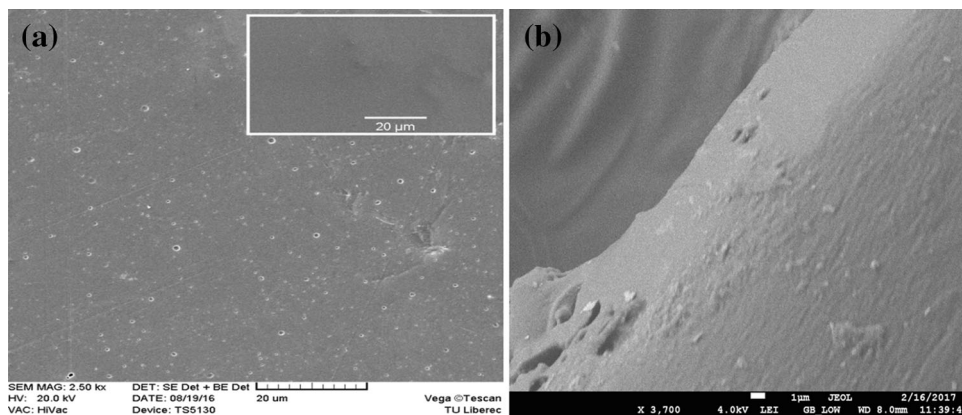
Fig. 2 FTIR spectra of pure PVA and RGO-PVA nanocomposite films

in tensile strength and moduli of the samples is observed in the present study. The above results declare a strong interfacial interaction due to the hydrogen bond formation between residual oxygen-functional groups in RGO and –OH molecules of PVA chain [29]. The XRD analysis of the present study also suggests the uniform dispersion of the RGO nanosheets into PVA matrix at molecular level.

3.3 SEM and FE SEM analysis

Figure 3a represents phase morphology of pure PVA and 0.020% (w/w) RGO-doped PVA film. The inset shows surface morphology of pure PVA sample. The images indicate that surfaces of both pure PVA and RGO doped PVA samples are smooth and regular. Figure 3b represents FE SEM cross-sectional image of 0.020% (w/w) RGO-doped PVA sample. The images show the exfoliation and well dispersion of RGO nanosheets into PVA matrix.

Fig. 3 **a** SEM micrograph of 0.020% (w/w) RGO-doped PVA film. The inset is a pure PVA film micrograph, and **b** FE SEM cross-sectional micrograph of 0.020% (w/w) RGO-doped PVA film



3.4 Optical characterization

3.4.1 Optical absorbance

Figure 4 indicates the absorption spectra of both pure PVA and RGO-doped PVA nanocomposites. On loading RGO nanosheets, the color of PVA film changed from transparent to slightly blackish. The graph showed that absorption is exponential for PVA nanocomposites and drastic for pure PVA. It was also observed that absorbance decreased up to 390 nm. The pure PVA spectrum exhibited no absorption peak in the visible region. It had a main peak at 279.7 nm and a weak shoulder peak at 333.7 nm. The main peak was due to absorption transition $\pi \rightarrow \pi^*$ and the shoulder peak was attributed to $n \rightarrow \pi^*$ transition [30, 31]. After adding RGO nanosheets, there appeared a very broad peak in the UV region. The shifting of pure PVA peak might be due to hydrogen bond formation between PVA hydroxyl groups and RGO nanosheets [29]. The formation of these new bonds into the nanocomposites might be responsible for change in crystallinity, enhancement of mechanical strength and tuning the optical properties of nanocomposites.

3.4.2 Absorption edge, direct/indirect band gap and Urbach energy

Figure 5a represents the effect of incident photon energy ($h\nu$) on absorption coefficient (α) of pure PVA and RGO-doped PVA films. It is evident from the plot that PVA absorption edge acquires lower values of photon energy by loading RGO nanosheets in the PVA matrix. This obviously specifies that optical band gap of polymer lowers with higher doping concentrations. The value of absorption edge was calculated by extrapolating initial linear portion of $(\alpha-h\nu)$ plot curve to zero α value [10]. Figure 5b describes the plot of $(\alpha h\nu)^2$ versus incident photon energy

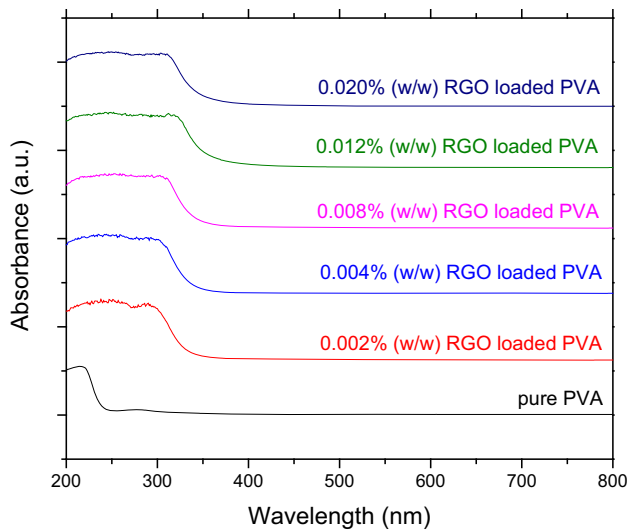


Fig. 4 Optical absorbance as a function of wavelength for pure PVA and RGO–PVA nanocomposite films

$(h\nu)$ of pure PVA and RGO-doped PVA nanocomposite films for calculating direct band gap. The direct band gap was achieved by extrapolating the initial linear portion of the plot curve to zero $(\alpha h\nu)^2$ value. Figure 5c shows the plot of $(\alpha h\nu)^{1/2}$ versus $(h\nu)$ for calculating indirect band gap of the nanocomposites. The same procedure was adopted for calculating direct/indirect band gap. The Urbach energy was calculated using slope of linear portion of the $\ln(\alpha)$ versus $(h\nu)$ plot, shown in Fig. 5d. The values of direct/indirect band gap of pure PVA and RGO–PVA nanocomposites at different RGO loadings are shown in Fig. 5e. The effect of RGO doping on absorption edge and Urbach energy is shown in Fig. 5f. By incorporating a very small quantity of RGO nanosheets (0.012 wt%), there observed a rational change in absorption edge (5.14–3.26 eV), direct band gap (5.29–3.59 eV), indirect band gap (4.95–3.20 eV) and Urbach energy (0.2–0.85 eV) of PVA nanocomposites. The observed changes indicate that the energy band structure of pure PVA is modified actually. The decrease in band gap and increase in band tail are directly linked to contents of incorporated RGO nanosheets. The doped RGO nanosheets can create the localized energy states in the band gap region, which can work as recombination and trapping hubs. The recombination and trapping centers narrow down the band gap region and widen the band tails, resulting in shifting the Fermi level [32].

3.4.3 Refractive index

Figure 6a displays variation in extinction coefficients with incident wavelength of pure PVA and RGO–PVA samples. Figure 6b displays variation in refractive index with wavelength of the prepared samples. A sharp decrease in

refractive index is observed for pure PVA sample with initial increasing wavelengths, whereas dispersion attitude is observed for the nanocomposites. The refractive index of the nanocomposites is higher than that of pure PVA. It is also observed that on increasing RGO loadings, refractive index of the samples increases. Increasing RGO loadings in PVA matrix can cause the formation of hydrogen bonds between –OH group of PVA and RGO nanosheets. Interatomic distance drops and, hence, density and refractive index rise. Incorporating RGO nanosheets into PVA matrix may be liable for creating localized states in the band gap region, thus increasing the density. These states boost the lower energy transections and are responsible for producing change in refractive index of the samples [33].

3.4.4 Optical dielectric constant

Optical dielectric constant is related to the density of states (DOS) present in the band gap region, so it is useful in band structure analysis of the nanocomposites. Figure 7a shows the real part and Fig. 7b shows imaginary part of dielectric constant. By increasing the contents of RGO nanosheets, both parts of dielectric constant are enhancing. More concentration of nanofiller means generation of more DOS in the band gap region. As a result, polarization increases, causing the increment in dielectric constant. Figure 7a shows that PVA nanocomposites show dispersion behavior below 490 nm, and then become smooth. For lower wavelengths, the nanocomposites pursue the applied field fluctuations. But at larger wavelengths, the nanocomposite molecules cannot pursue the field fluctuation because of their inertia. The similar behavior is noticed for imaginary part (or optical loss) of dielectric constant. For lower wavelengths, the optical loss rises because of dipole polarization and for longer wavelengths dipole polarizations grows weak [17]. This dispersion plays a key role in the field of optical communication and in designing the optical devices.

3.4.5 Optical conductivity

Figure 8 displays optical conductivity as a function of wavelength for the prepared samples. By increasing RGO contents, optical conductivity rises. It can be observed that optical conductivity rises at lower wavelengths (higher photon energy), due to the high absorbance of the samples in this region and ability of photons to excite electrons. The RGO nanosheets are well dispersed into PVA matrix spaces during dispersion process. As a result, a segregated network is generated, charge carriers are increased and so the conductivity [17].

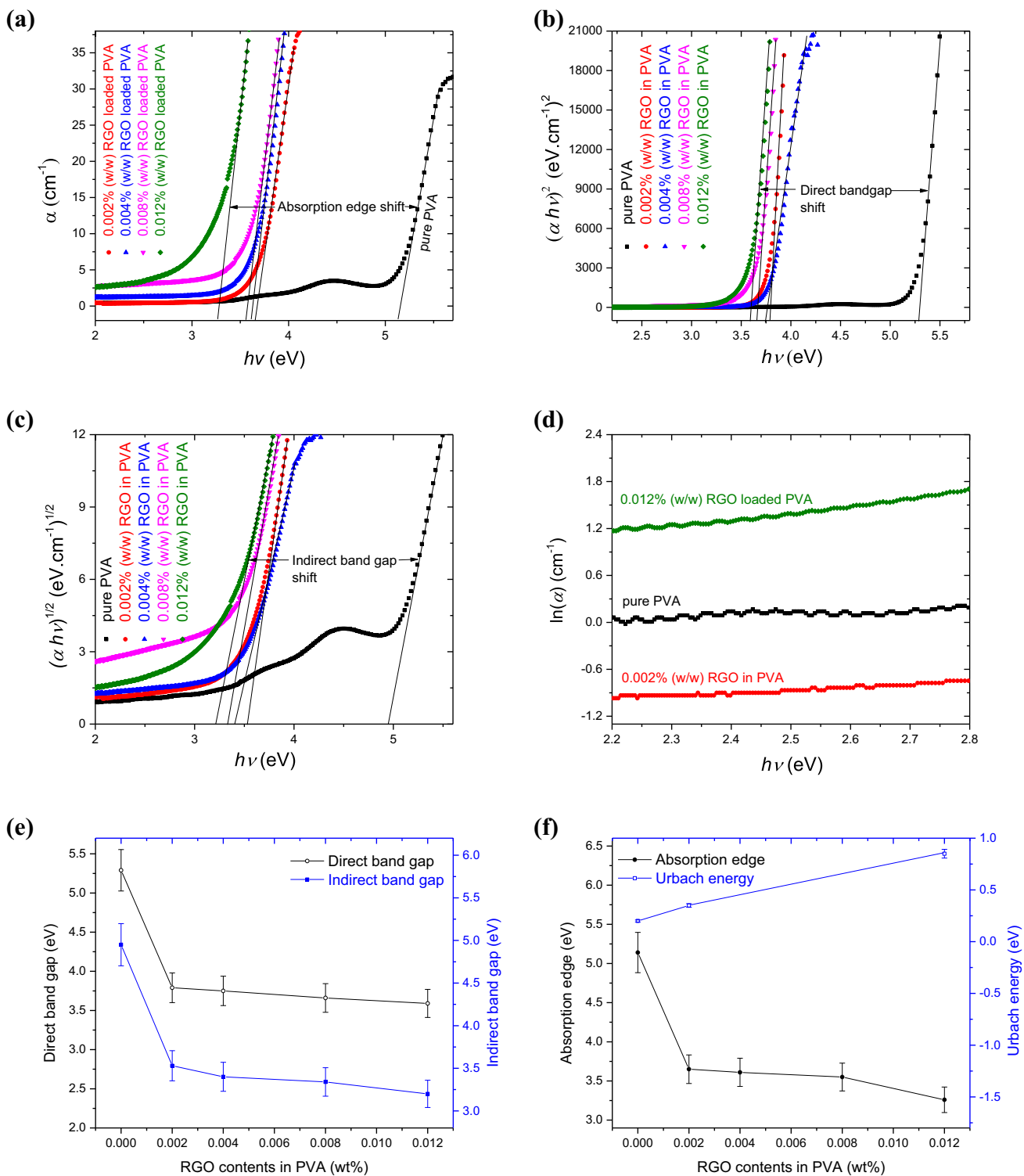


Fig. 5 a Effect of incident photon energy ($h\nu$) on absorption coefficient (α) of pure PVA and RGO–PVA samples, **b** $(\alpha h\nu)^2$ versus ($h\nu$) plot of the prepared nanocomposites, **c** $(\alpha h\nu)^{1/2}$ versus ($h\nu$) plot for the samples, **d** $\ln(\alpha)$ versus ($h\nu$) plot of the nanocomposites,

e direct and indirect band gap at different RGO loadings, and **f** effect of RGO doping on absorption edge and Urbach energy of pure PVA and RGO–PVA nanocomposite films

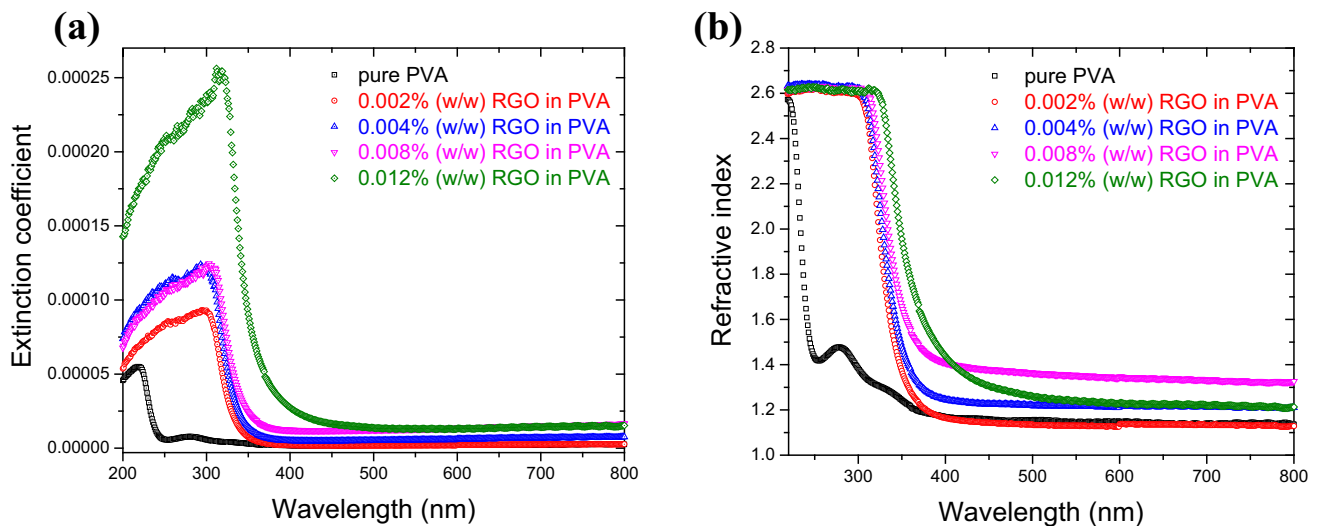


Fig. 6 Representative of **a** extinction coefficient versus wavelength, and **b** refractive index versus wavelength of pure PVA and RGO–PVA nanocomposites

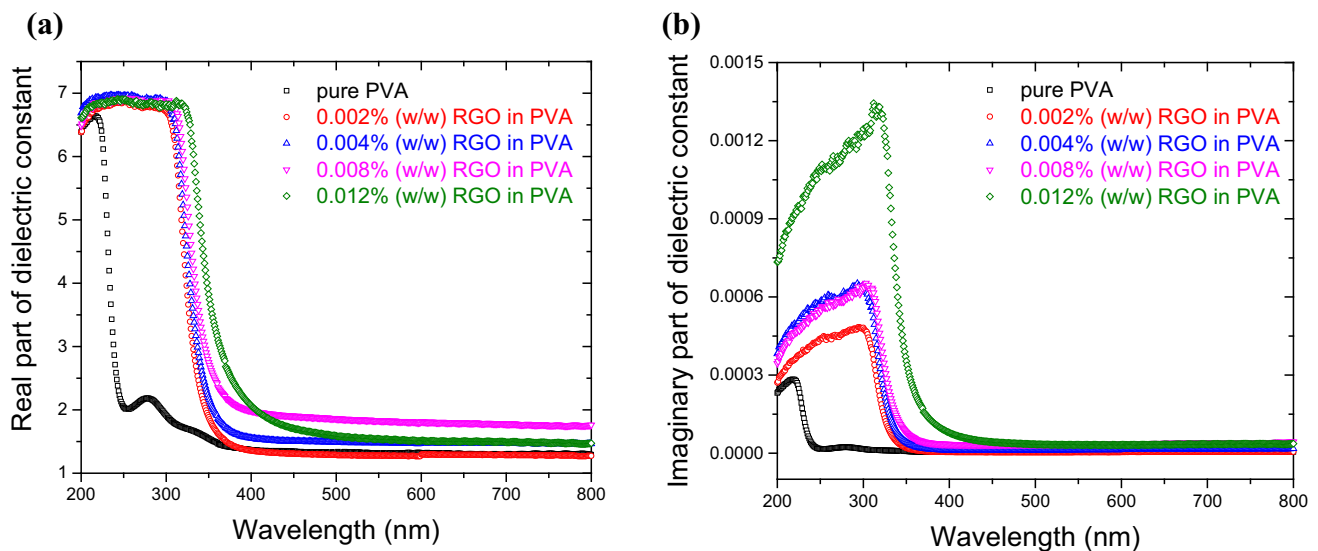


Fig. 7 **a** Real part of dielectric constant versus wavelength, and **b** imaginary part of dielectric constant versus wavelength of pure PVA and RGO–PVA nanocomposites

3.4.6 Dispersion parameters

The dispersion of refractive index is an interesting feature. To explore refractive index dispersion, Wemple and DiDomenico formulated a single oscillator model [34]. According to this model, an empirical formula for analyzing dispersion of refractive index is as follows:

$$n^2 = 1 + \frac{E_0 E_d}{E_0^2 - (hv)^2}, \quad (7)$$

where E_0 , E_d and hv are oscillator energy (average band gap), dispersion energy (optical transition strength) and incident photon energy, respectively. Figure 9a displays

$(n^2 - 1)^{-1}$ versus $(hv)^2$ plot for the samples. Parameters E_0 and E_d were calculated using intercept and slope of the proportional region of the graph, near the absorption edge. The intercept is equivalent to (E_0/E_d) and slope is equivalent to $-(E_0 E_d)^{-1}$. The tabulated values of E_0 and E_d as a function of RGO loading are displayed in Fig. 9b. It is interesting to note that the W–D model tabulated values of E_0 are approximately equal to direct band gap values obtained by Tauc's plot of the samples. Both models confirmed the decreasing behavior of band gap values upon increasing RGO contents. Figure 9b displays that dispersion energy increases with increasing contents of RGO nanosheets into PVA matrix, so optical transition strength

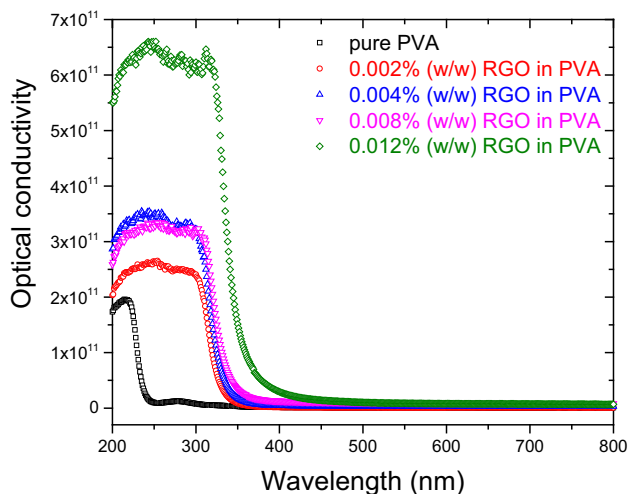


Fig. 8 Optical conductivity versus wavelength of the samples

improves due to the generation of charge transfer complex between RGO and PVA matrix. Hence, degree of disorder grows up [17].

3.5 Mechanical characterization

Figure 10a represents typical stress–strain plots of pure PVA and RGO–PVA samples. The trend of plot curves of the figure indicate that pure PVA film is soft and elastic, whereas the RGO–PVA nanocomposites are comparatively hard and brittle. Figure 10b shows the effect of loading RGO nanosheets on tensile strength and percentage elongation at break of the prepared nanocomposites. Figure 10c describes the effect of incorporating RGO nanosheets on Young’s moduli of the nanocomposites along with theoretical modeling curves. The figure shows that tensile

strength (Fig. 10a) and Young’s moduli (Fig. 10c) of nanocomposites were enhanced, whereas the elongation at break (Fig. 10b) decreased on incorporating RGO nanosheets into PVA matrix. This typical trend is reported in the earlier literature as well [5, 29, 35, 36]. The Young’s moduli of the nanocomposites were calculated using linear fitting of initial linear portion of load–gauge length plot, of the experimental data. By adding just 0.020% (w/w) of RGO nanosheets in the PVA matrix, the nanocomposite got higher strain rate and its tensile strength was increased from 26.6 MPa of pure PVA to 45.6 MPa and the Young’s modulus increased from 144 MPa of pure PVA to 162 MPa. The experimental data curve was compared with both H–T and mixture rule model curves. The H–T model is frequently used for the prediction of Young’s modulus of nanofiller-incorporated composites. This model assumes that the nanofiller might be distributed randomly or parallel along surface of polymer films. For random and parallel orientation of RGO nanosheets, the nanocomposite modulus E_{random} and $E_{parallel}$, respectively, were calculated using following equations given below [5, 29, 36, 37]:

$$E_{random} = E_{PVA} \left[\frac{3}{8} \frac{1 + \eta_L \xi V_C}{1 - \eta_L V_C} + \frac{5}{8} \frac{1 + 2\eta_T V_C}{1 - \eta_T V_C} \right], \tag{8}$$

$$E_{parallel} = E_{PVA} \left[\frac{1 + \eta_L \xi V_C}{1 - \eta_L V_C} \right], \tag{9}$$

$$\eta_L = \left[\frac{\frac{E_{RGO}}{E_{PVA}} - 1}{\frac{E_{RGO}}{E_{PVA}} + \xi} \right], \tag{10}$$

$$\eta_T = \left[\frac{\frac{E_{RGO}}{E_{PVA}} - 1}{\frac{E_{RGO}}{E_{PVA}} + 2} \right], \tag{11}$$

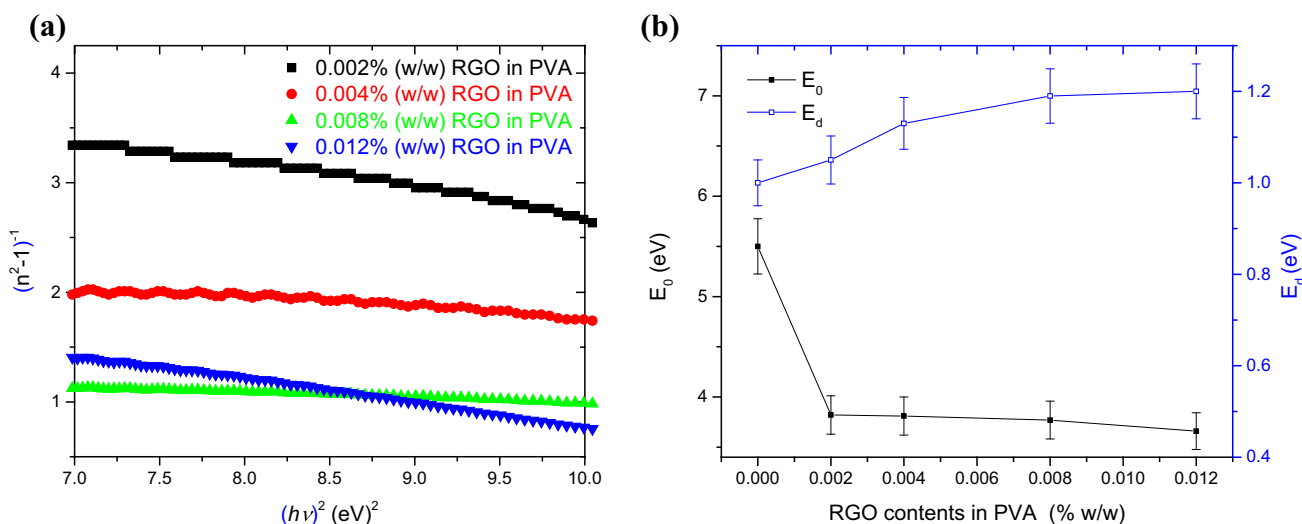


Fig. 9 a $(n^2 - 1)^{-1}$ versus $(hv)^2$ plot of pure PVA and RGO–PVA nanocomposites, and b the values of E_0 and E_d at different RGO contents

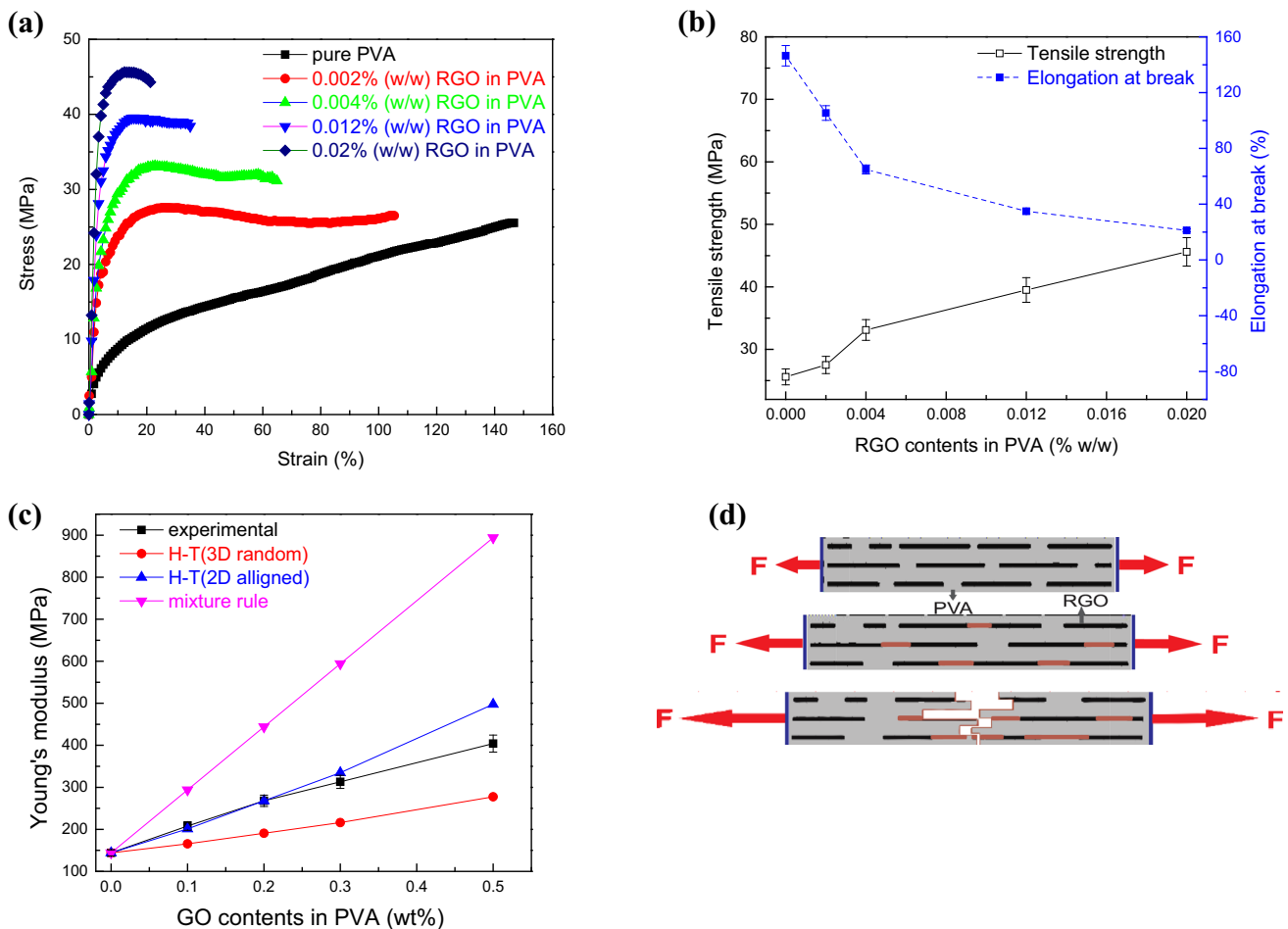


Fig. 10 **a** Stress–strain curve of pure PVA and RGO–PVA nanocomposites at different RGO loadings, **b** tensile strength and elongation at break of the nanocomposites at different loadings, **c** experimental data

curve, H–T random and parallel curves, and mixture rule curve of nanocomposites at different RGO loadings, and **d** fracture mechanism of the nanocomposites

$$\zeta = \left[\frac{2 l_{RGO}}{3 t_{RGO}} \right], \tag{12}$$

where E_{PVA} , E_{RGO} , V_C , l_{RGO} and t_{RGO} are Young’s modulus of pure PVA, Young’s modulus of RGO nanosheets, volume fraction of the nanocomposites, length and thickness of RGO nanosheets, respectively. The Young’s modulus of RGO nanosheets was 0.25 TPa [5]. The Young’s modulus of pure PVA was calculated as 144 MPa from the experiment. The length and thickness of RGO nanosheets were taken from our previous study [9]. The weight contents of nanofiller were converted into volume fraction using following equation:

$$V_C = \frac{W \rho_{PVA}}{W \rho_{PVA} + (1 - W) \rho_{RGO}}, \tag{13}$$

where W , ρ_{PVA} , and ρ_{RGO} symbolize the weight contents, density of pure PVA and density of RGO nanosheets, respectively. The density of pure PVA and RGO nanosheets is 1.3 and 2.2 g cm⁻³, respectively [5]. Replacing

parametric values into relevant equations, H–T predicted Young’s moduli of nanocomposite films were calculated under mentioned assumptions and shown in Fig. 10c. The Young’s moduli of RGO–PVA nanocomposites were also predicted using a simple tactic of rule of mixtures [35]. This approach is suitable for graphene-filled polymers, parallel alignment of graphene sheets, uniform strain over whole nanocomposite and delivers an upper bound of Young’s modulus. The Young’s moduli of the nanocomposites (E_c) were calculated using the following equation and shown in Fig. 10c:

$$E_c = V_C E_{RGO} + (1 - V_C) E_{PVA}. \tag{14}$$

Figure 10c indicates that experimentally calculated data points for Young’s moduli of pure PVA and RGO–PVA nanocomposites and these are in good agreement with H–T (parallel) predicted calculations. Furthermore, the figure confirms that RGO nanosheets are aligned parallel to films surfaces. The constancy of experimental data points shows that external load was transferred successfully to

RGO nanosheets at RGO–PVA interface, through robust interactions and assumed that RGO nanosheets were aligned along the samples surface [34]. The enhanced mechanical properties of RGO–PVA nanocomposites might be due to the excellent mechanical properties of individual RGO nanosheets and residual oxygen-functional groups of RGO nanosheets that produce strong molecular interaction among polymer chains [36]. The relative crystallinity has direct influence on mechanical properties of PVA. The XRD analysis has proved that on incorporating RGO nanosheets, the relative crystallinity has improved substantially and, as a result, strength with brittleness is induced into the nanocomposites, as shown in Fig. 10b. The XRD, FTIR and SEM analyses showed the strong uniform dispersion of RGO nanosheets into PVA matrix, suggesting the enhanced tensile strength and Young's moduli of the nanocomposites. Yang et al. [20] prepared PVA/graphene 3.5% (w/w) nanocomposite and showed that the tensile strength was increased by 32% and Young's modulus by 16% as compared to pure PVA. Li et al. [18] prepared rGO/PVA 0.1% (w/w) nanofiber and reported that the tensile strength and Young's modulus were increased by 20.6 and 20.8%, respectively. Zhao et al. [38] reported that graphene/PVA (1.8 v%) nanocomposite enhanced 150% tensile strength and 10 times Young's modulus. Bao et al. [25] reported that PVA/graphene-0.8 sample showed 66% increase in tensile strength and for PVA/graphene-0.4 sample and 70% increase in Young's modulus.

In general, the transmission of tensile load from PVA matrix to RGO nanosheets is strongly reliant on interfacial interaction between wrapping matrix and nanosheets, uniform dispersion of nanosheets at molecular level, hydrogen bonding between polymer chains and oxygen-functional groups of nanosheets and, finally, large aspect ratio of RGO nanosheets. Consequently, there is a prominent enhancement in tensile strength and Young's moduli of the nanocomposites. The fracture mechanism of the nanocomposites is described in Fig. 10d. When the sample is stretched under the effect of an external force, the adjacent RGO nanosheets start slipping. The polymer chains provide bridging and stop further slipping. On further stretching, the covalently coupled RGO nanosheets with PVA polymer chains are stretched in the direction of force with dissipation of large amount of energy. The hydrogen bonding between RGO nanosheets and PVA molecular chains is broken slowly. When external force exceeds the breaking stress, the π -conjugated system of nanocomposite is destroyed and brittle fracture takes place [39].

Overall, the XRD analysis was performed to investigate the crystallinity and uniform dispersion of RGO nanosheets into PVA matrix. The characteristic peak of individual RGO nanosheets at $2\theta = 23.19^\circ$ was disappeared after

dispersion into PVA matrix and the height of nanocomposite peaks at about $2\theta = 20^\circ$ was increased. It suggested the uniform dispersion of RGO nanosheets into PVA matrix and increased relative crystallinity of the nanocomposites. The presence of –OH stretching vibrations and shifting of this peak toward lower wavenumbers in FTIR spectra indicated the strong hydrogen bonding and interfacial interaction between the RGO nanosheets and the PVA matrix. The SEM micrographs also showed that RGO nanosheets were uniformly dispersed into the PVA matrix. The XRD, FTIR and SEM analyses provided evidence on uniform dispersion of RGO nanosheets which might be resulted in the enhancement of mechanical and optical properties of the PVA nanocomposites. The relative crystallinity of nanocomposites of the present study was increased from 23.7 to 39.6%. UV–visible spectra revealed that absorbance was increased with RGO loadings; consequently, the band structure parameters of the nanocomposites were modified. The absorption edge and direct optical band gap of 0.012% (w/w) RGO–PVA nanocomposite were reduced from 5.14 to 3.26 eV and 5.29 to 3.59 eV, respectively, as compared to pure PVA matrix. The indirect band gap and Urbach energy for the same sample were modified from 4.95 to 3.20 eV and 0.20 to 0.85 eV, respectively. The refractive index and optical conductivity were significantly enhanced. Tauc's and W–D models reported nearly the same values of optical band gap. The tensile strength of 0.020% (w/w) RGO–PVA nanocomposite was increased from 25.6 to 45.6 MPa, whereas the Young's modulus increased from 144 to 162 MPa, as compared to pure PVA matrix. Both H–T and mixture rule models reinforced the experimentally calculated Young's moduli results. The present study proved that the structural, optical and mechanical properties of the prepared nanocomposites were changed entirely.

4 Conclusions

The RGO–PVA nanocomposites were successfully prepared via solution casting. Some drastic changes in structural, optical and mechanical properties of the PVA matrix were observed by incorporating small quantities of RGO nanosheets as dopant. The uniform dispersion of nanosheets at molecular level without restacking of nanosheets resulted in strong intermolecular hydrogen bonding. This made the nanocomposites tunable with remarkably improved mechanical and optical properties. The mechanical strength, band tail, refractive index and optical conductivity of the nanocomposites increased, whereas the direct/indirect band gap decreased with increasing doping contents. The reduction in optical band gap of PVA might lead to develop a new material for organic solar cell and

biosensors. The dispersion of refractive index might lead to use the nanocomposites in optical communication and designing of dispersion devices. Such incredible nanocomposites need to be investigated for more optoelectronics applications.

Compliance with ethical standards

Conflict of interest The authors have no potential conflict of interest.

References

1. J. Pyun, K. Matyjaszewski, *Chem. Mater.* **13**, 3436–3448 (2001)
2. M.K. El-Mansy, E.M. Sheha, K.R. Patel, G.D. Sharma, *Optik* **124**, 1624–1631 (2013)
3. M.H. Makled, E. Sheha, T.S. Shanap, M.K. El-Mansy, *J. Adv. Res.* **4**, 531–538 (2013)
4. C.L. Wu, M.Q. Zhang, M.Z. Rong, K. Friedrich, *Compos. Sci. Technol.* **62**, 1327–1340 (2002)
5. J. Liang, Y. Huang, L. Zhang, Y. Wang, Y. Ma, T. Guo, Y. Chen, *Adv. Funct. Mater.* **19**, 2297–2302 (2009)
6. C. Lee, X. Wei, J.W. Kysar, J. Hone, *Science* **321**, 385–388 (2008)
7. L. Liu, A.H. Barber, S. Nuriel, H.D. Wagner, *Adv. Funct. Mater.* **15**, 975–980 (2005)
8. A.N. Ananth, S. Umapathy, J. Sophia, T. Mathavan, D. Mangalaraj, *Appl. Nanosci.* **1**, 87–96 (2011)
9. M. Aslam, M.A. Kalyar, Z.A. Raza, *Mater. Res. Express* **3**, 105036 (2016). doi:[10.1088/2053-1591/3/10/105036](https://doi.org/10.1088/2053-1591/3/10/105036)
10. F.F. Muhammad, S.B. Aziz, S.A. Hussein, *J. Mater. Sci. Mater. Electron.* **26**, 521–529 (2015)
11. S. Elliot, *The Physics and Chemistry of Solids* (Wiley, New York, 1998)
12. P.P. Sahay, R.K. Nath, S. Tewari, *Cryst. Res. Technol.* **42**, 275–280 (2007)
13. E.A. Davis, N.F. Mott, *Philos. Mag.* **22**, 0903–0922 (1970)
14. J. Tauc, A. Menth, D.L. Wood, *Phys. Rev. Lett.* **25**, 749–752 (1970)
15. P.K. Khare, S.K. Jain, *B. Mater. Sci.* **23**, 17–21 (2000)
16. F. Urbach, *Phys. Rev.* **92**, 1324 (1953)
17. O.G. Abdullah, S.B. Aziz, K.M. Omer, Y.M. Salih, *J. Mater. Sci. Mater. Electron.* **26**, 5303–5309 (2015)
18. J. Li, L. Shao, X. Zhou, Y. Wang, *RSC Adv.* **4**, 43612–43618 (2014)
19. J.H. Hong PO-DA, H. Wu, *J. Appl. Polym. Sci.* **69**, 2477–2486 (1998)
20. X. Yang, L. Li, S. Shang, X.M. Tao, *Polymer* **51**, 3431–3435 (2010)
21. S.K. Sharma, J. Prakash, P.K. Pujari, *Phys. Chem. Chem. Phys.* **17**, 29201–29209 (2015)
22. Y. Xu, W. Hong, H. Bai, C. Li, G. Shi, *Carbon* **47**, 3538–3543 (2009)
23. Y. Kojima, A. Usuki, M. Kawasumi, A. Okada, Y. Fukushima, T. Karauchi, O. Kamigaito, *Mater. Res.* **8**, 1185–1189 (1993)
24. T. Tyler, O. Shenderova, G. Cunningham, J. Walsh, J. Drobnik, G. McGuire, *Diam. Relat. Mater.* **15**, 2078–2081 (2006)
25. C. Bao, Y. Guo, L. Song, Y. Hu, *J. Mater. Chem.* **21**, 13942–13950 (2011)
26. S. Gahlot, P.P. Sharma, V. Kulshrestha, P.K. Jha, A.C.S. Appl. Mater. Inter. **6**, 5595–5601 (2014)
27. L. Lu, H. Sun, F. Peng, Z. Jiang, *J. Membr. Sci.* **281**, 245–252 (2006)
28. Y. Chen, X. Zhang, P. Yu, Y. Ma, *Chem. Commun.* **30**, 4527–4529 (2009)
29. H.K. Cheng, N.G. Sahoo, Y.P. Tan, Y. Pan, H. Bao, L. Li, S.H. Chan, J. Zhao, A.C.S. Appl. Mater. Interfaces **4**, 2387–2394 (2012)
30. A.M. Shehap, *Egypt. J. Solids* **31**, 75–91 (2008)
31. D.M. Sabara, J.S. Dunne, A.Q. Pedro, J. Trifunovic, I.I. Balogun, O. Kotlicic, A. Serrano, I. Kertesz, *Biotechnol. Food Sci.* **75**, 39–49 (2011)
32. M.M. El-Nahass, M. Dongol, M. Abou-Zied, A. El-Denglawey, *Physica B Condens Matter.* **368**, 179–187 (2005)
33. I. Saini, J. Rozra, N. Chandak, S. Aggarwal, P.K. Sharma, A. Sharma, *Mater. Chem. Phys.* **139**, 802–810 (2013)
34. S.H. Wemple, M. DiDomenico Jr., *Phys. Rev. B* **3**, 1338–1351 (1971)
35. Z. Li, R.J. Young, I.A. Kinloch, *ACS Appl. Mater. Interfaces.* **5**, 456–463 (2013)
36. R.R. Tiwari, K.C. Khilar, U. Natarajan, *J. Appl. Polym. Sci.* **108**, 1818–1828 (2008)
37. J.B. Gao, M.E. Itkis, A.P. Yu, E. Bekyarova, B. Zhao, R.C. Haddon, *J. Am. Chem. Soc.* **127**, 3847–3854 (2005)
38. X. Zhao, Q. Zhang, D. Chen, P. Lu, *Macromolecules* **43**, 2357–2363 (2010)
39. S. Gong, M. Wu, L. Jiang, Q. Cheng, *Mater. Res. Express* **3**, 075002 (2016)